This paper appears in Control Engineering Practice, 2022.
https://doi.org/10.1016/j.conengprac.2022.105186

VDC-Based Admittance Control of Multi-DOF Manipulators Considering Joint Flexibility via Hierarchical Control Framework

Liang Ding[a], Hongjun Xing[a,b,*], Haibo Gao[a], Ali Torabi[b], Weihua Li[a], Mahdi Tavakoli[b]

[a]*State Key Laboratory of Robotics and System, Harbin Institute of Technology, Harbin 150001, China*
[b]*Department of Electrical and Computer Engineering, University of Alberta, Edmonton T6G 1H9, Alberta, Canada*

Abstract

Multi-degree-of-freedom (Multi-DOF) manipulators have shown a high potential for enhancing the flexibility and performance of robotic manipulations. However, the presence of unknown disturbance, including uncertain dynamics and external forces/torques, makes the control of a multi-DOF manipulator rather complicated, and the stability of the robotic system is hard to be guaranteed. In this paper, a virtual decomposition control (VDC)-based admittance control approach for multi-DOF manipulators has been proposed considering joint flexibility via hierarchical control framework. The joint flexibility is solved by a separate adaptive controller different from the manipulator's links. The high-level admittance controller is built upon a low-level VDC-based inner control loop, which can deal with the complicated system dynamics (including the joint friction and joint flexibility) and modeling uncertainty. The external force/torque (F/T) is estimated with a generalized momentum-based interaction force estimation technique; thereby avoiding the cost of wrist F/T sensors. The robotic system's stability has been guaranteed in both free-space motions and constrained motions using the specific features of VDC (proof of each subsystem's *virtual stability*). The advantages and effectiveness of the proposed method in tuning the robot-environment dynamic behavior are demonstrated through experiments.

Keywords: Multi-DOF manipulators, virtual decomposition control (VDC), admittance control, joint flexibility, stability analysis.

1. Introduction

Multi-degree-of-freedom (Multi-DOF) manipulators have been widely employed in many areas, including door opening in constrained environments, human-robot interaction, and surgical applications (Karayiannidis et al., 2016; Xing et al., 2019; Chen and Ro, 2022; Torabi et al., 2019). The employment of multi-DOF manipulators in addressing tasks with contact with the environment has excellent advantages because they can be reconfigured and adapted to yield the best task performance. In Carriere et al. (2019), a semi-autonomous robotic assistant was proposed for ultrasound scanning using a multi-DOF manipulator, where the position of the probe was driven using an admittance controller. In Ficuciello et al. (2015), a control approach with multi-DOF manipulators was proposed to enhance the robots' operational performance for human-robot physical interaction by enlarging the stability region in the impedance parameters space. Many other potential application areas can be found in hydraulic manipulators, mobile manipulators, and dual-arm systems (Koivumäki et al., 2019; Mai and Wang, 2014; Han et al., 2019). However, a practical compliance control approach for multi-DOF manipulators with high control bandwidth is not provided yet.

The compliance control approach is fascinating for enabling the robot and its environment to behave in a compliant manner. Two fundamental methods are proposed based on hybrid position/force control (Raibert and Craig, 1981) and impedance control (Hogan, 1985). Impedance control and admittance control are two ways of implementing impedance control, depending on the causality of the controller (Ott et al., 2010). In contrast to impedance control, admittance control has the advantage of easily adapting to the up-to-date industrial robot system, namely, a position-control/velocity-control system; however, its implementation bandwidth is limited by the inherent position/velocity controller. In Xing et al. (2021), an admittance control method of mobile manipulators was proposed for human-robot interaction; however, it was conducted at the velocity level, and the robot dynamics was neglected. In Zhuang et al. (2019), a torque-sensing-based admittance controller was presented to achieve human-robot synchronization, the reference velocity severed as the input of a low-level PD controller. Yet, the system's stability was not guaranteed. Successful completion of these interactive tasks requires that the robotic system precisely controls its interaction with the environment with a high control bandwidth. Thus, the complex system dynamics should be properly handled.

It is common for industrial manipulators to have flexibility in their joints, and this contributes greatly to their dynamic control. In Ghorbel et al. (1989), the first adaptive control approach of flexible-joint manipulators with the assumption of weak-joint elasticity was presented. In Fateh (2012), a robust tracking controller of flexible-joint manipulators

*Corresponding author
Email addresses: liangding@hit.edu.cn (Liang Ding), xinghj@hit.edu.cn (Hongjun Xing), gaohaibo@hit.edu.cn (Haibo Gao), ali.torabi@ualberta.ca (Ali Torabi), liweihua@hit.edu.cn (Weihua Li), mahdi.tavakoli@ualberta.ca (Mahdi Tavakoli)

was developed using voltage control strategy, where a novel uncertainty estimation approach was introduced. However, only simulation verification was provided. In Ma et al. (2021), an adaptive fuzzy control strategy was presented for flexible-joint manipulators. The nonlinearity was solved by a fuzzy-logic algorithm. Nonetheless, this approach was only applicable to a single-link manipulator, and no real-time implementation was attempted. Also, many model-free methods were proposed for manipulators with flexible joints (Kim et al., 2019; Yuan et al., 2020; Du et al., 2021).

For force control of multi-DOF systems, the abundant DOFs makes the system's nonlinear dynamics rather complicated. From the view of online implementation, the traditional dynamic control methods, like Lagrangian formulation (Hollerbach, 1980) and Newton–Euler formulation (Buondonno and De Luca, 2015), cannot be effectively employed, suffering from the high computational load and parameter uncertainty. Furthermore, the robotic system's stability in contact environment should also be considered because the contact dynamics can be severe if the robot dynamics are not treated adequately (Xing et al., 2022).

The control challenges mentioned above have led to the employment of a nonlinear model-based control method, where a well-designed feedforward control term can partially address the system's nonlinearities. However, the exact feedforward dynamic model of multi-DOF manipulators is hard or even impossible to derive due to the severe joint coupling and nonlinear friction (Ficuciello et al., 2014). In Zhu (2010), an adaptive nonlinear model-based control approach was proposed called virtual decomposition control (VDC) to model and control multi-DOF robotic systems inspired by the Newton–Euler formulation. The primary concept of this approach is to virtually decompose the entire robotic system into several independent subsystems. Each subsystem is connected with the contiguous subsystem through the "force" element composed of force/torque (F/T) and the "velocity" element comprised of linear velocity and angular velocity. The dynamic interaction between the adjacent subsystems is described using the unique feature of VDC called virtual power flow (VPF). Compared with the dynamic model based on the Lagrangian formulation, this method's computation is proportional to the number of the subsystems (the calculation of the Lagrangian high-order dynamic model is proportional to the fourth power of the system's DOF (Zhu, 2010)). Therefore, the computational efficiency improves significantly.

With its stunning performance in dealing with complex robotic systems, VDC has been highlighted with many applications involving multi-DOF systems, including electrically driven manipulators (Zhu et al., 1998; Zhu and Lamarche, 2007; Zhu et al., 2013), mobile manipulators (Antonelli et al., 2004; Jafarinasab et al., 2019), and exoskeleton robots (Luna et al., 2016; Ochoa Luna et al., 2015). A hybrid force/position control framework with smooth transition phases from free-space motion to constrained motion based on VDC was achieved, yet, a commercial end-effector force sensor was required (Zhu and De Schutter, 2002). In Xia et al. (2019), a dynamic model for a 6-DOF manipulator was established with consideration of joint elasticity and friction based on VDC. This modeling approach's effectiveness has been experimentally verified, but they failed to provide a corresponding control method for their model. In Koivumäki and Mattila (2017), an impedance control method for multi-DOF hydraulic manipulators was proposed with highly nonlinear dynamics solved, which guaranteed the L_2 and L_∞ stability of the system in both free space and contact environment. However, the inertial term of the impedance model was neglected, and the joint friction was not addressed. In Asl et al. (2021), an adaptive neural networks-based control scheme was presented for robotic exoskeletons to obtain the desired transparency, while joint flexibility was not considered.

The problem with much of the literature about dynamic control of complex robotic systems is that when the number of DOFs increases, the computational load will increase rapidly; hence, online implementation is extraordinarily challenging (Koivumäki and Mattila, 2017; Sciavicco and Siciliano, 2012). Besides, the unknown dynamic parameters, nonlinear frictions, and elasticity of the robotic system also present great difficulty in controlling the system (Wang, 2016; Sharifi et al., 2020; Madsen et al., 2020). The model-based adaptive control approach and model-free method have been widely used in dealing with complicated joint flexibility. However, a complete-dynamics-based control of multi-DOF manipulators integrated with flexible joints for experimental implementation and stability proof was not provided.

This paper proposes a novel VDC-based admittance control approach for multi-DOF manipulators integrated with flexible joints via a hierarchical control framework. The main contributions of this paper are as follows: 1) A novel non-switching stability-guaranteed admittance control method is proposed for multi-DOF manipulators considering joint flexibility using a hierarchical design framework; 2) the admittance controller based on the inner motion control loop is designed using virtual decomposition theory, the joint friction and flexibility are specially handled by a VDC-based adaptive controller, where the joint stiffness coefficient is also self-adapted; 3) rigorous stability proof and motion/force convergence proof are presented for multi-DOF manipulators to cover both unconstrained and constrained motions. The benefit of VDC is that each subsystem can be independently controlled to reduce computation and the entire system's stability can simultaneously be guaranteed.

The remainder of this paper is organized as follows. Section 2 presents the kinematic and dynamic models for Multi-DOF manipulators based on VDC. The proposed hierarchical control framework for compliant behavior and singularity avoidance via VDC is described in Section 3. Section 4 provides the stability proof of the approach. Experiments that demonstrate the validity and performance of the proposed method are presented in Section 5. Section 6 concludes the manuscript.

2. VDC-Based Modeling of Multi-DOF Manipulators

In this section, the kinematic and dynamic models of multi-DOF manipulators are provided. Section 2.1 presents the

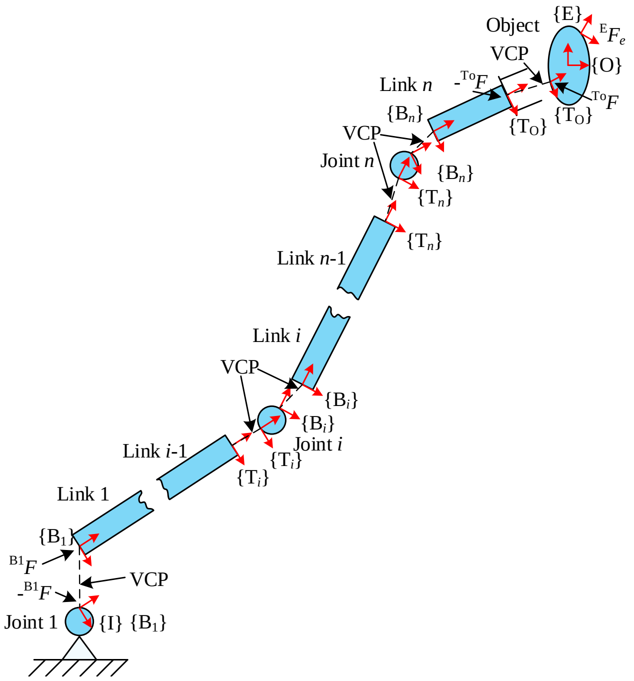

Figure 1: Virtual decomposition of an n-DOF manipulator.

kinematic model of the manipulators, and their dynamic model is shown in Section 2.2.

2.1. Kinematic Modeling of Multi-DOF Manipulators

Fig. 1 shows the virtual decomposition of an n-DOF manipulator. The entire manipulator system is virtually decomposed into $2n + 1$ subsystems, including n joints, n links, and an object. As shown in Fig. 1, $2n$ virtual cutting points (VCPs) $(\mathrm{B}_1, \cdots, \mathrm{B}_n, \mathrm{T}_2, \cdots, \mathrm{T}_n, \mathrm{T}_\mathrm{O})$ have been defined (the definition of VCP is shown below). Frame $\{\mathrm{T}_\mathrm{O}\}$ is located at the connection point between the n^{th} link and the object. Also, frame {E} is located at the point where the contact occurs. It should be emphasized that the object has only one VCP.

The concept of VCP is of great importance to the VDC approach because it can conceptually decompose a complex robotic system into several subsystems, which is defined in Definition 1.

Definition 1. *A cutting point is a directed separation interface that conceptually cuts through a rigid body. The two parts caused by the virtual cut share equal pose. The cutting point is expressed as a driving cutting point by one part and is simultaneously expressed as a driven cutting point by the other part. The force/moment vector is exerted from which the cutting point is expressed as a driving cutting point to which the cutting point is expressed as a driven cutting point.*

Here, the term of linear/angular velocity and force/torque transformations will be introduced. Consider {A} as a frame attached to a rigid body. Let ${}^{\mathrm{A}}v \in \mathbb{R}^3$ and ${}^{\mathrm{A}}\omega \in \mathbb{R}^3$ be the linear and angular velocity vectors of frame {A}, and the linear/angular velocity vector of frame {A} is written as ${}^{\mathrm{A}}V = \left[{}^{\mathrm{A}}v^{\mathrm{T}},\ {}^{\mathrm{A}}\omega^{\mathrm{T}}\right]^{\mathrm{T}}$. Similarly, let ${}^{\mathrm{A}}f \in \mathbb{R}^3$ and ${}^{\mathrm{A}}m \in \mathbb{R}^3$ be the force and torque vectors of frame {A}, and the F/T vector of frame {A} is written as ${}^{\mathrm{A}}F = \left[{}^{\mathrm{A}}f^{\mathrm{T}},\ {}^{\mathrm{A}}m^{\mathrm{T}}\right]^{\mathrm{T}}$. Then, consider two frames, expressed as {A} and {B}, being fixed to a rigid body, no matter whether it is moving or subject to physical force and torque vectors. The following relations hold

$$ {}^{\mathrm{B}}V = {}^{\mathrm{A}}U_{\mathrm{B}}^{\mathrm{T}}\,{}^{\mathrm{A}}V, \quad {}^{\mathrm{A}}F = {}^{\mathrm{A}}U_{\mathrm{B}}\,{}^{\mathrm{B}}F, \tag{1} $$

where ${}^{\mathrm{A}}U_{\mathrm{B}} \in \mathbb{R}^{6\times 6}$ is an F/T transformation matrix that transforms the F/T vector expressed in frame {B} to the same F/T vector expressed in frame {A}.

Thus, the linear/angular velocity vector of each manipulator's subsystem in its corresponding frame can be expressed as

$$
\begin{aligned}
{}^{\mathrm{B}_1}V &= z\dot{q}_1, \\
{}^{\mathrm{T}_i}V &= {}^{\mathrm{B}_{i-1}}U_{\mathrm{T}_i}^{\mathrm{T}}\,{}^{\mathrm{B}_{i-1}}V, \\
{}^{\mathrm{B}_i}V &= z\dot{q}_i + {}^{\mathrm{T}_i}U_{\mathrm{B}_i}^{\mathrm{T}}\,{}^{\mathrm{T}_i}V = z\dot{q}_i + {}^{\mathrm{B}_{i-1}}U_{\mathrm{B}_i}^{\mathrm{T}}\,{}^{\mathrm{B}_{i-1}}V, \\
{}^{\mathrm{T}_\mathrm{O}}V &= {}^{\mathrm{B}_n}U_{\mathrm{T}_\mathrm{O}}^{\mathrm{T}}\,{}^{\mathrm{B}_n}V, \\
{}^{\mathrm{O}}V &= {}^{\mathrm{T}_\mathrm{O}}U_{\mathrm{O}}^{\mathrm{T}}\,{}^{\mathrm{T}_\mathrm{O}}V, \\
{}^{\mathrm{E}}V &= {}^{\mathrm{O}}U_{\mathrm{E}}^{\mathrm{T}}\,{}^{\mathrm{O}}V,
\end{aligned} \tag{2}
$$

where $i = 2, 3, \ldots, n$, $z = [0, 0, 0, 0, 0, 1]^{\mathrm{T}} \in \mathbb{R}^6$, $\dot{q}_i$ represents the angular velocity of the i^{th} joint, and ${}^{\mathrm{T}}U_{\mathrm{B}}$ denotes the force/moment transformation matrix from {B} to {T} with its definition in (1).

The task-space velocity vector ${}^{\mathrm{E}}V \in \mathbb{R}^6$ and the joint velocity vector $\dot{q} = [\dot{q}_1, \ldots, \dot{q}_n]^{\mathrm{T}} \in \mathbb{R}^n$ are controlled by a Jacobian matrix $J \in \mathbb{R}^{6\times n}$ as follows,

$$ {}^{\mathrm{E}}V = J\dot{q} = \left[{}^{\mathrm{B}_1}U_{\mathrm{E}}^{\mathrm{T}}z, {}^{\mathrm{B}_2}U_{\mathrm{E}}^{\mathrm{T}}z, \ldots, {}^{\mathrm{B}_n}U_{\mathrm{E}}^{\mathrm{T}}z\right]\dot{q}. \tag{3} $$

It is worth mentioning that the reference frame of the Jacobian J is the contact point frame {E}.

2.2. Dynamic Modeling of Multi-DOF Manipulators

Consider a rigid object with frame {A} fixed; then, the general formulation of its dynamics, in which frame {A} is used as the reference frame, can be expressed as

$$ M_{\mathrm{A}}\frac{\mathrm{d}}{\mathrm{d}t}({}^{\mathrm{A}}V) + C_{\mathrm{A}}({}^{\mathrm{A}}\omega){}^{\mathrm{A}}V + G_{\mathrm{A}} = {}^{\mathrm{A}}F^{*}, \tag{4} $$

where $M_{\mathrm{A}} \in \mathbb{R}^{6\times 6}$ is the mass matrix, $C_{\mathrm{A}}({}^{\mathrm{A}}\omega) \in \mathbb{R}^{6\times 6}$ is the matrix of Coriolis and centrifugal terms, $G_{\mathrm{A}} \in \mathbb{R}^6$ is the gravity term, and ${}^{\mathrm{A}}F^{*} \in \mathbb{R}^6$ is the net F/T vector of the rigid body expressed in frame {A}.

According to (4), the force resultant equations of the n links and the object can be calculated as

$$
\begin{aligned}
{}^{\mathrm{O}}F^{*} &= {}^{\mathrm{O}}U_{\mathrm{T}_\mathrm{O}}\,{}^{\mathrm{T}_\mathrm{O}}F - {}^{\mathrm{O}}U_{\mathrm{E}}\,{}^{\mathrm{E}}F_e, \\
{}^{\mathrm{B}_n}F^{*} &= {}^{\mathrm{B}_n}F - {}^{\mathrm{B}_n}U_{\mathrm{T}_\mathrm{O}}\,{}^{\mathrm{T}_\mathrm{O}}F, \\
{}^{\mathrm{T}_i}F &= {}^{\mathrm{T}_i}U_{\mathrm{B}_i}\,{}^{\mathrm{B}_i}F, \quad i = n, \ldots, 2, \\
{}^{\mathrm{B}_i}F^{*} &= {}^{\mathrm{B}_i}F - {}^{\mathrm{B}_i}U_{\mathrm{T}_{i+1}}\,{}^{\mathrm{T}_{i+1}}F, \quad i = n-1, \ldots, 1,
\end{aligned} \tag{5}
$$

where ${}^{\mathrm{E}}F_e \in \mathbb{R}^6$ is the external F/T vector exerted at the contact point {E} and ${}^{\mathrm{A}}F \in \mathbb{R}^6$, $A \in \{\mathrm{T_O}, \mathrm{B}_i, \mathrm{T}_i\}$, denotes the driving F/T vector of each link at its corresponding frame. The purpose of (5) is to calculate the driving F/T vector from each joint to the next link, ${}^{\mathrm{B}_i}F$, according to (4), via an iterative approach.

The dynamics of all manipulator joints are also considered to improve the modeling accuracy. It is worth mentioning that for most conventional manipulator joints, their transmission system is usually mixed with transmission elasticity, motor inertia, and friction (Ren et al., 2018). In the case of a flexible manipulator joint, when taking the friction term on both the motor and link sides and the joint elasticity into account, the dynamic model is expressed as (Spong, 1987)

$$\begin{aligned} \tau_{fi}(\dot{q}_i) &= \tau_{ti} - \tau_{ai}, \\ \tau_{ti} &= k_{fi}(\phi_i - q_i), \\ I_{mi}\ddot{\phi}_i + \tau_{f\phi i}(\dot{\phi}_i) &= \tau_i - \tau_{ti}, \end{aligned} \tag{6}$$

where $i = 1, \ldots, n$, τ_{fi} denotes the link-side friction torque, τ_{ti} is the effective transmission input torque, I_{mi} denotes the joint moment of inertia, ϕ_i represents the motor-side joint position, $\tau_{f\phi i}$ denotes the motor-side friction torque, τ_i represents the motor control torque, k_{fi} is the joint stiffness coefficient, and

$$\tau_{ai} = z^{\mathrm{T}}\,{}^{\mathrm{B}_i}F \tag{7}$$

denotes the torque output of the i^{th} joint toward the corresponding link.

The friction torques τ_{fi} and $\tau_{f\phi i}$ are assumed as

$$\begin{aligned} \tau_{fi}(\dot{q}_i) &= f_{vqi}\dot{q}_i + f_{cqi}\mathrm{sign}(\dot{q}_i), \\ \tau_{f\phi i}(\dot{\phi}_i) &= f_{v\phi i}\dot{\phi}_i + f_{c\phi i}\mathrm{sign}(\dot{\phi}_i), \end{aligned} \tag{8}$$

where f_{vqi} and f_{cqi} denote the link-side viscous and Coulomb friction coefficients of the i^{th} joint, $f_{v\phi i}$ and $f_{c\phi i}$ represent its motor-side viscous and Coulomb friction coefficients.

3. Hierarchical Control Framework for Compliant Behavior via VDC

The primary target of this section is to design an appropriate admittance controller to realize the desired user-defined compliant behavior for a flexible-joint manipulator. We are starting with the presentation of a robot-environment interaction force estimation method to generate the signal input for the admittance controller in Section 3.1. In Section 3.2, a high-level admittance controller integrated with the low-level VDC is designed, where an adaptive controller is proposed for joint friction and flexibility within the low-level controller.

3.1. Robot-Environment Interaction Force/Torque Estimation

The robot-environment interaction-related F/T of the admittance controller can be obtained either by using a commercial wrist F/T sensor or estimation approach (Mohammadi et al., 2013). When there is no wrist sensor available at the end-effector, an alternative method of obtaining the interaction can be provided based on joint torque measurements.

For a manipulator with flexible joints, if the joint torque sensor is integrated; then, we can take advantage of the joint torque measurements instead of working with the full dynamics of the robot mixed with joint elasticity. This method can avoid the requirement of (ϕ_i, $\dot{\phi}_i$, $\ddot{\phi}_i$), I_{mi}, $\tau_{f\phi i}(\dot{\phi}_i)$; thus, the force estimation accuracy will be enhanced (Liu et al., 2019). Actually, when a high-resolution position encoder and a joint torque sensor are equipped on the motor side and the link side of a joint, respectively, the joint link-side position can be calculated as $q = \phi - \tau_t/k_f$.

The complete dynamic model of an n-DOF manipulator considering link-side joint friction can be expressed as

$$M(q)\ddot{q} + C(q, \dot{q})\dot{q} + G(q) + \tau_f(q, \dot{q}) = \tau + J^{\mathrm{T}}\,{}^{\mathrm{E}}F_e, \tag{9}$$

where $M(q) \in \mathbb{R}^{n\times n}$, $C(q, \dot{q}) \in \mathbb{R}^{n\times n}$, and $G(q) \in \mathbb{R}^n$ denote the inertia matrix, Coriolis and centrifugal terms, and gravity term of the entire robotic system, respectively, $\tau_f(q, \dot{q}) \in \mathbb{R}^n$ denotes the joint friction torque vector, and $\tau \in \mathbb{R}^n$ denotes the joint control torque vector. It should be noted that the contact F/T ${}^{\mathrm{E}}F_e$ is usually measured using a wrist sensor placed at the end-effector. Here, a generalized momentum-based interaction force estimation method (De Luca et al., 2006) is adopted to avoid the requirement of a wrist F/T sensor.

According to Siciliano et al. (2010), in (9), $\dot{M}(q) - 2C(q, \dot{q})$ is a skew-symmetric matrix, and with symmetry of $M(q)$, it is obvious that

$$\dot{M}(q) = C(q, \dot{q}) + C^{\mathrm{T}}(q, \dot{q}). \tag{10}$$

To circumvent the measurement of joint acceleration, which is difficult if not impossible, a practical interaction force estimation approach with joint torque measurements according to generalized momentum (De Luca et al., 2006) is proposed. The generalized momentum is expressed as

$$p = M(q)\dot{q}. \tag{11}$$

The time evolution of p can be obtained as

$$\dot{p} = \dot{M}(q)\dot{q} + M(q)\ddot{q}, \tag{12}$$

and combining (9), (10), and (12) yields

$$\dot{p} = C^{\mathrm{T}}(q, \dot{q})\dot{q} - G(q) - \tau_f(q, \dot{q}) + \tau + J^{\mathrm{T}}\,{}^{\mathrm{E}}F_e. \tag{13}$$

Then, the interaction force-related joint torque is observed using

$$r(t) = K_I\Big(p - \int_0^t (\tau + C^{\mathrm{T}}(q, \dot{q})\dot{q} - G(q) - \tau_f(q, \dot{q}) + r)\mathrm{d}\tau\Big), \tag{14}$$

where K_I is a positive gain matrix. The dynamic evolution of $r(t)$ has a stable structure as

$$\dot{r}(t) = K_I(J^{\mathrm{T}}\,{}^{\mathrm{E}}F_e - r). \tag{15}$$

If the gain matrix K_I is chosen sufficiently massive, then we can obtain the estimate of the joint torque resulting from the interaction force as

$$J^{\mathrm{T}}\,{}^{\mathrm{E}}F_e \approx r. \tag{16}$$

According to (16), the estimated interaction F/T ${}^{\mathrm{E}}\hat{F}_e$ can be calculated as

$$ {}^{\mathrm{E}}\hat{F}_e = (J^{\mathrm{T}}(q))^{\dagger} r, \tag{17} $$

where $(.)^{\dagger}$ denotes the Moore-Penrose pseudoinverse of a matrix. To estimate the robot-environment interaction, τ is measured by joint torque sensors, the manipulator parameters related to $M(q)$, $C(q,\dot{q})$, $G(q)$, and $\tau_f(q,\dot{q})$ can be estimated by experiment (Calanca et al., 2010; Gaz et al., 2019). Here, the joint friction model for $\tau_f(q,\dot{q})$ is simplified as (8), which only relates to its corresponding joint position and velocity (Calanca et al., 2010). It is noteworthy that the linearized joint friction model in (8) is only applicable when the joint motion is small (Xing et al., 2021); if the joint motion is on a large scale, a more elaborated joint friction model is required.

3.2. Admittance Controller Design Based on Low-Level VDC

The required end-effector velocity considering interaction force is proposed in Section 3.2.1, followed by the VDC-based subsystem control of the compliant object, links, and joints, respectively.

3.2.1. Design of Required End-Effector Velocity with Compliance Considered

According to Hogan (1985), the desired task-space admittance model for a manipulator is expressed as[1]

$$ f_d - f_e = M_d(\ddot{x} - \ddot{x}_d) + D_d(\dot{x} - \dot{x}_d) + K_d(x - x_d), \tag{18} $$

where $M_d \in \mathbb{R}^{3\times3}$, $D_d \in \mathbb{R}^{3\times3}$, and $K_d \in \mathbb{R}^{3\times3}$ are diagonal positive-definite matrices characterizing the desired inertia, damping, and stiffness; $f_d \in \mathbb{R}^3$ and $f_e \in \mathbb{R}^3$ are the desired and actual external forces, thus, f_e represents the force component of ${}^{\mathrm{E}}\hat{F}_e$ in the first equation of (5), which can be estimated via (17); and $x_d \in \mathbb{R}^3$ and $x \in \mathbb{R}^3$ are the desired and actual end-effector trajectories at the contact point, respectively. In this paper, the orientation of the manipulator's end-effector will be invariable unless orientation compliance is taken into account.

The terminology of required velocity is an essential concept in the VDC approach, including the desired velocity and one or more terms related to the control errors, such as position errors and force errors.

Inspired by Koivumäki and Mattila (2017), the required velocity for the manipulator $\dot{x}_r$ is designed as

$$ \dot{x}_r = \dot{x}_d + \Lambda_a(x_d - x) + \Lambda_b(\ddot{x}_d - \ddot{x}) + \Lambda_c(f_d - f_e), \tag{19} $$

where $\Lambda_a \in \mathbb{R}^{3\times3}$, $\Lambda_b \in \mathbb{R}^{3\times3}$, $\Lambda_c \in \mathbb{R}^{3\times3}$ are three diagonal positive-definite matrices. The values of the diagonal positive-definite matrices are defined as

$$ \Lambda_c = D_d^{-1}, \quad \Lambda_a = K_d D_d^{-1}, \quad \Lambda_b = M_d D_d^{-1}. \tag{20} $$

[1]Here, the admittance model is only for the position adjustment of the manipulator under the action of the external force. The compliant orientation adjustment can be easily achieved via a similar method with external torque, which will be demonstrated in the experiment to make the paper concise.

With the proposed control law (19) and the parameter definition in (20), the control law (19) equals the target admittance (18).

The matrices M_d, D_d, and K_d are all diagonal positive-definite, thus it derives

$$ \begin{aligned} D_d^{-1}\Lambda_a D_d &= \Lambda_a, \quad & D_d^{-1}\Lambda_b D_d &= \Lambda_b, \\ D_d K_d D_d^{-1} &= K_d, \quad & D_d M_d D_d^{-1} &= M_d. \end{aligned} \tag{21} $$

According to (18)-(21), it yields

$$ \begin{aligned} \dot{x}_r =& \dot{x}_d + \Lambda_a(x_d - x) + \Lambda_b(\ddot{x}_d - \ddot{x}) \\ &+ \Lambda_c(M_d(\ddot{x} - \ddot{x}_d) + D_d(\dot{x} - \dot{x}_d) + K_d(x - x_d)) \\ =& \dot{x}_d + \Lambda_c D_d(\dot{x} - \dot{x}_d) + \Lambda_a(x_d - x) \\ &+ \Lambda_b(\ddot{x}_d - \ddot{x}) + \Lambda_c(M_d(\ddot{x} - \ddot{x}_d) + K_d(x - x_d)) \\ =& \dot{x}_d + D_d^{-1} D_d(\dot{x} - \dot{x}_d) + \Lambda_a(x_d - x) + \Lambda_b(\ddot{x}_d - \ddot{x}) \\ &+ D_d^{-1}\Lambda_b D_d(\ddot{x} - \ddot{x}_d) + D_d^{-1}\Lambda_a D_d(x - x_d) \\ =& \dot{x}. \end{aligned} \tag{22} $$

Combining (19)-(22) yields

$$ \begin{aligned} & f_d - f_e \\ =& \Lambda_c^{-1}(\dot{x}_r - \dot{x}_d) - \Lambda_c^{-1}\Lambda_a(x_d - x) \\ &- \Lambda_c^{-1}\Lambda_b(\ddot{x}_d - \ddot{x}) \\ =& D_d K_d D_d^{-1}(x - x_d) + D_d(\dot{x}_r - \dot{x}_d) \\ &+ D_d M_d D_d^{-1}(\ddot{x}_d - \ddot{x}) \\ =& K_d(x - x_d) + D_d(\dot{x}_r - \dot{x}_d) + M_d(\ddot{x}_d - \ddot{x}), \end{aligned} \tag{23} $$

where the last row is equal to (18).

With the obtained required end-effector velocity, we will design the independent controllers for each subsystem using VDC framework.

3.2.2. Control of Compliant Object

The linear/angular velocity vector ${}^{\mathrm{E}}V \in \mathbb{R}^6$ of the contact point in frame {E} is written as

$$ {}^{\mathrm{E}}V = T\dot{x} \tag{24} $$

with $T = [I_{3\times3}, 0_{3\times3}]^{\mathrm{T}} \in \mathbb{R}^{6\times3}$, meaning no angular velocity is applied to the contact point. Then the velocity vector for the object can be obtained using the last equation of (2). Here, $\dot{x} \in \mathbb{R}^3$ represents the end-effector's task-space velocity vector, derived in (18).

The F/T vector of the contact point expressed in {E} is derived as

$$ {}^{\mathrm{E}}F_e = T f_e; \tag{25} $$

then, the net F/T vector of the object can be derived as the first row of (5). Here, $f_e \in \mathbb{R}^3$ represents the robot-environment interaction force vector.

Similar to (24), the required velocity at the contact point in {E} is expressed as

$$ {}^{\mathrm{E}}V_r = T\dot{x}_r, \tag{26} $$

where $\dot{x}_r \in \mathbb{R}^3$ is defined in (19), and the required velocity for the object is

$$ {}^{\mathrm{O}}V_r = {}^{\mathrm{E}}U_{\mathrm{O}}^{\mathrm{T}\,\mathrm{E}}V_r. \tag{27}$$

Similar to (25), the required F/T at the contact point in {E} is expressed as

$$ {}^{\mathrm{E}}F_r = T f_d, \tag{28}$$

where $f_d \in \mathbb{R}^3$ is the desired task-space force vector in (18).

The required net force/moment vector for the object can be expressed as

$$ {}^{\mathrm{O}}F_r^* = Y_{\mathrm{O}}\hat{\theta}_{\mathrm{O}} + K_{\mathrm{O}}({}^{\mathrm{O}}V_r - {}^{\mathrm{O}}V) \tag{29}$$

with

$$ Y_{\mathrm{O}}\theta_{\mathrm{O}} = M_{\mathrm{O}}\frac{\mathrm{d}}{\mathrm{d}t}({}^{\mathrm{O}}V_r) + C_{\mathrm{O}}({}^{\mathrm{O}}\omega){}^{\mathrm{O}}V_r + G_{\mathrm{O}},$$

where $Y_{\mathrm{O}} \in \mathbb{R}^{6\times 13}$ is a regressor matrix, $\theta_{\mathrm{O}} \in \mathbb{R}^{13}$ and $\hat{\theta}_{\mathrm{O}} \in \mathbb{R}^{13}$ are the unknown parameter vector and its estimate, respectively, and $K_{\mathrm{O}} \in \mathbb{R}^{6\times 6}$ is a symmetric positive-definite matrix representing the velocity feedback control. Y_{O} is a function of the known parameters (measured or calculated), including $\frac{\mathrm{d}}{\mathrm{d}t}({}^{\mathrm{O}}V_r)$, ${}^{\mathrm{O}}V_r$, and ${}^{\mathrm{O}}V$. θ_{O} denotes a function of the unknown parameters, containing object mass, position of the mass center, and moment of inertia. The exact representation of each element of these parameters can be found in Zhu (2010).

The following projection function in Zhu (2010) is utilized for unknown parameter adaptation.

Definition 2. *A projection function $\mathcal{P}(s(t), k, a(t), b(t), t) \in \mathbb{R}$ is a differentiable scalar function defined in $t \geqslant 0$ such that its time derivative is governed by*

$$ \dot{\mathcal{P}} = ks(t)\kappa \tag{30}$$

with

$$ \kappa = \begin{cases} 0, & \text{if } \mathcal{P} \leqslant a(t) \text{ and } s(t) \leqslant 0 \\ 0, & \text{if } \mathcal{P} \geqslant b(t) \text{ and } s(t) \geqslant 0 \\ 1, & \text{otherwise} \end{cases}$$

where $s(t) \in \mathbb{R}$ is a scalar variable, k is a positive constant and $a(t) \leqslant b(t)$ holds.

Consider an arbitrary $\mathcal{P}$ function defined in (30)*, and for any constant $\mathcal{P}_c$ satisfying $a(t) \leqslant \mathcal{P}_c \leqslant b(t)$, it follows that*

$$ (\mathcal{P}_c - \mathcal{P})\Big(s(t) - \frac{1}{k}\dot{\mathcal{P}}\Big) \leqslant 0. \tag{31}$$

The estimated parameters of $\hat{\theta}_{\mathrm{O}}$ in (29) can be updated using the parameter adaptation method provided in Definition 2 with

$$ s_{\mathrm{O}} = Y_{\mathrm{O}}^{\mathrm{T}}({}^{\mathrm{O}}V_r - {}^{\mathrm{O}}V). \tag{32}$$

Then, each element of $\hat{\theta}_{\mathrm{O}}$ can be updated using (30) as

$$ \hat{\theta}_{\mathrm{O}\gamma} = \mathcal{P}(s_{\mathrm{O}\gamma}, \rho_{\mathrm{O}\gamma}, \underline{\theta}_{\mathrm{O}\gamma}, \overline{\theta}_{\mathrm{O}\gamma}, t), \forall \gamma \in [1, 13], \tag{33}$$

where $\hat{\theta}_{\mathrm{O}\gamma}$ is the γ^{th} element of $\hat{\theta}_{\mathrm{O}}$, $s_{\mathrm{O}\gamma}$ is the γ^{th} element of s_{O}, $\rho_{\mathrm{O}\gamma} > 0$ is the update gain, and $\underline{\theta}_{\mathrm{O}\gamma}$ and $\overline{\theta}_{\mathrm{O}\gamma}$ are the lower bound and the upper bound of $\theta_{\mathrm{O}\gamma}$.

Similar to the first equation of (5), the required net force/moment vector of the object can be calculated as

$$ {}^{\mathrm{O}}F_r^* = {}^{\mathrm{O}}U_{\mathrm{T_O}}{}^{\mathrm{T_O}}F_r - {}^{\mathrm{O}}U_{\mathrm{E}}{}^{\mathrm{E}}F_r. \tag{34}$$

3.2.3. Control of Links

The linear/angular velocity vector of the i^{th} link ${}^{\mathrm{B}_i}V \in \mathbb{R}^6$ can be obtained using the first three equations of (2), and its force/moment vector ${}^{\mathrm{B}_i}F \in \mathbb{R}^6$ can be derived using the last three equations of (5).

According to (3), the required joint velocity $\dot{q}_{ir}$ is expressed as

$$ \dot{q}_r = J^{\dagger\,\mathrm{E}}V_r, \tag{35}$$

where $\dot{q}_r = [\dot{q}_{1r}, \cdots, \dot{q}_{nr}]^{\mathrm{T}} \in \mathbb{R}^n$ denotes the required joint velocity vector.

The required velocity vector of the i^{th} link ${}^{\mathrm{B}_i}V \in \mathbb{R}^6$ is expressed as

$$\begin{aligned} {}^{\mathrm{B}_1}V_r &= z\dot{q}_{1r}, \\ {}^{\mathrm{T}_i}V_r &= {}^{\mathrm{B}_{i-1}}U_{\mathrm{T}_i}^{\mathrm{T}\;\mathrm{B}_{i-1}}V_r, \\ {}^{\mathrm{B}_i}V_r &= z\dot{q}_{ir} + {}^{\mathrm{T}_i}U_{\mathrm{B}_i}^{\mathrm{T}\;\mathrm{T}_i}V_r = z\dot{q}_{ir} + {}^{\mathrm{B}_{i-1}}U_{\mathrm{B}_i}^{\mathrm{T}\;\mathrm{B}_{i-1}}V_r. \end{aligned} \tag{36}$$

The required F/T vector of the i^{th} link ${}^{\mathrm{B}_i}F \in \mathbb{R}^6$ can be obtained as

$$\begin{aligned} {}^{\mathrm{B}_n}F_r^* &= {}^{\mathrm{B}_n}F_r - {}^{\mathrm{B}_n}U_{\mathrm{T_O}}{}^{\mathrm{T_O}}F_r, \\ {}^{\mathrm{T}_i}F_r &= {}^{\mathrm{T}_i}U_{\mathrm{B}_i}{}^{\mathrm{B}_i}F_r, \quad i = n, \ldots, 2, \\ {}^{\mathrm{B}_i}F_r^* &= {}^{\mathrm{B}_i}F_r - {}^{\mathrm{B}_i}U_{\mathrm{T}_{i+1}}{}^{\mathrm{T}_{i+1}}F_r, \quad i = n-1, \ldots, 1. \end{aligned} \tag{37}$$

The VDC-based control procedure for the links is the same as the process for the object in (29) and (32)-(34) with appropriate frame substitutions.

3.2.4. Control of Joints

The relationship between the joint velocity vector and the linear/angular velocity vector of the adjacent links is shown in the first three equations of (2). The dynamics of the i^{th} joint is provided by (6), where the joint elasticity is considered.

Combined with (37), the commanded joint torque of the i^{th} joint is designed as

$$\begin{aligned} \tau_{tid} &= Y_{ai}\hat{\theta}_{ai} + z^{\mathrm{T}\;\mathrm{B}_i}F_r + k_{vqi}(\dot{q}_{ir} - \dot{q}_i), \\ \phi_{ir} &= \tau_{tid}/\hat{k}_{fi} + q_{ir}, \\ \tau_i &= \tau_{tid} + Y_{bi}\hat{\theta}_{bi} + k_{v\phi i}(\dot{\phi}_{ir} - \dot{\phi}_i), \end{aligned} \tag{38}$$

with

$$\begin{aligned} Y_{ai} &= [\dot{q}_{ir},\ \mathrm{sign}(\dot{q}_{ir})], & \theta_{ai} &= [f_{vqi},\ f_{cqi}]^{\mathrm{T}}; \\ Y_{bi} &= [\ddot{\phi}_{ir},\ \dot{\phi}_{ir},\ \mathrm{sign}(\dot{\phi}_{ir})], & \theta_{bi} &= [I_{mi},\ f_{v\phi i},\ f_{c\phi i}]^{\mathrm{T}}. \end{aligned} \tag{39}$$

Define

$$\begin{aligned} s_{ai} &= Y_{ai}^{\mathrm{T}}(\dot{q}_{ir} - \dot{q}_i), \\ s_{bi} &= Y_{bi}^{\mathrm{T}}(\dot{\phi}_{ir} - \dot{\phi}_i), \\ s_{kfi} &= (\phi_{ir} - q_{ir})[(\dot{\phi}_{ir} - \dot{\phi}_i) - (\dot{q}_{ir} - \dot{q}_i)], \end{aligned} \tag{40}$$

then, each element of $\hat{\theta}_{ai}$, $\hat{\theta}_{bi}$, and $\hat{k}_{fi}$ can be updated using (30), respectively, as

$$\begin{aligned} \hat{\theta}_{ai\gamma} &= \mathcal{P}(s_{ai\gamma}, \rho_{ai\gamma}, \underline{\theta}_{ai\gamma}, \overline{\theta}_{ai\gamma}, t), \forall\gamma \in \{1, 2, 3\}, \\ \hat{\theta}_{bi\gamma} &= \mathcal{P}(s_{bi\gamma}, \rho_{bi\gamma}, \underline{\theta}_{bi\gamma}, \overline{\theta}_{bi\gamma}, t), \forall\gamma \in \{1, 2\}, \\ \hat{k}_{fi} &= \mathcal{P}(s_{kfi}, \rho_{kfi}, \underline{k}_{fi}, \overline{k}_{fi}, t), \end{aligned} \tag{41}$$

where $\hat{\theta}_{ai\gamma}$, $\hat{\theta}_{bi\gamma}$, $s_{ai\gamma}$, and $s_{bi\gamma}$ denote the γ^{th} element of $\hat{\theta}_{ai}$, $\hat{\theta}_{bi}$, s_{ai}, and s_{bi}, respectively; $\rho_{ai\gamma}$, $\rho_{bi\gamma}$, and ρ_{kfi} represent positive parameter update gains; $\underline{\theta}_{ai\gamma}$ and $\overline{\theta}_{ai\gamma}$ are the lower and upper bounds of $\theta_{ai\gamma}$; $\underline{\theta}_{bi\gamma}$ and $\overline{\theta}_{bi\gamma}$ denote the lower and upper bounds of $\theta_{bi\gamma}$; and $\underline{k}_{fi}$ and $\overline{k}_{fi}$ are the lower and upper bounds of k_{fi}.

The entire control system is shown in Fig. 2.

4. Stability Analysis

This section presents the stability proof of the designed control approach. Sections 4.1, 4.2, and 4.3 provide the *virtual stability* of the compliant object, links, and joints, respectively. Section 4.4 proves the stability of the entire manipulator based on the *virtual stability* of each subsystem.

First, we present the concept of VPF and *virtual stability*. The unique feature of the VDC approach is the introduction of VPF (defined in Definition 3). A VPF is defined and used to characterize the dynamic interactions among the subsystems, and plays an important role in leading to the theorem of *virtual stability*, which will be presented in Definition 4 (Koivumäki and Mattila, 2017).

Definition 3. *With respect to a frame $\{A\}$, the VPF is defined as the inner product of the linear/angular velocity vector error and the F/T vector error as*

$$p_{\mathrm{A}} \overset{def}{=} ({}^{\mathrm{A}}V_r - {}^{\mathrm{A}}V)^{\mathrm{T}}({}^{\mathrm{A}}F_r - {}^{\mathrm{A}}F), \tag{42}$$

where ${}^{\mathrm{A}}V_r \in \mathbb{R}^6$ and ${}^{\mathrm{A}}F_r \in \mathbb{R}^6$ represent the required vectors of ${}^{\mathrm{A}}V \in \mathbb{R}^6$ and ${}^{\mathrm{A}}F \in \mathbb{R}^6$, respectively.

Definition 4. *A subsystem with a driven VCP to which frame $\{A\}$ is attached and a driving VCP to which frame $\{C\}$ is attached is said to be virtually stable with its affiliated vector $x(t)$ being a virtual function in L_∞ and its affiliated vector $y(t)$ being a virtual function in L_2 , if and only if there exists a nonnegative accompanying function*

$$\nu(t) \geqslant \frac{1}{2}x(t)^{\mathrm{T}}Px(t), \tag{43}$$

such that

$$\dot{\nu}(t) \leqslant -y(t)^{\mathrm{T}}Qy(t) + p_{\mathrm{A}} - p_{\mathrm{C}} - s(t), \tag{44}$$

which is subject to

$$\int_0^\infty s(t)\mathrm{d}t \geqslant -\gamma_s \tag{45}$$

with $0 \leqslant \gamma_s < \infty$, where P and Q are two positive-definite matrices.

4.1. Virtual Stability of Compliant Object

Theorem 1. *Consider the compliant object described by* (4), (5), (18), (24), (25), *combined with its respective control equations* (19), (26)-(29), (34), *and with the parameter adaptation algorithms* (32) *and* (33). *The compliant object is virtually stable.*

Proof. Define the nonnegative accompanying function for the object ν_{O} as

$$\begin{aligned}\nu_{\mathrm{O}} =& \frac{1}{2}({}^{\mathrm{O}}V_r - {}^{\mathrm{O}}V)^{\mathrm{T}}M_{\mathrm{O}}({}^{\mathrm{O}}V_r - {}^{\mathrm{O}}V)\\ &+ \frac{1}{2}\sum_{\gamma=1}^{13}\frac{(\theta_{\mathrm{O}\gamma} - \hat{\theta}_{\mathrm{O}\gamma})^2}{\rho_{\mathrm{O}\gamma}},\end{aligned} \tag{46}$$

then, the time derivative of (46) can be obtained as

$$\dot{\nu}_{\mathrm{O}} \leqslant -({}^{\mathrm{O}}V_r - {}^{\mathrm{O}}V)^{\mathrm{T}}K_{\mathrm{O}}({}^{\mathrm{O}}V_r - {}^{\mathrm{O}}V) + p_{\mathrm{T_O}} - p_{\mathrm{E}}, \tag{47}$$

where $p_{\mathrm{T_O}}$ is the VPF (defined in Definition 3) at the driven VCP of the object, and p_{E} is the VPF between the object and the environment.

It is noteworthy that the compliant object of the manipulator only has one VCP (shown in Fig. 1), but two VPFs appear in (47). The VPF $p_{\mathrm{T_O}}$ locates at the VCP attached to frame $\{\mathrm{T_O}\}$ of the object. Therefore, for the *virtual stability* of the compliant object, the condition to guarantee that the existence of VPF p_{E} still satisfies Definition4 must be found.

According to (18), (19), (24)-(26), (28), and (42), it yields

$$\begin{aligned}p_{\mathrm{E}} =&({}^{\mathrm{E}}V_r - {}^{\mathrm{E}}V)^{\mathrm{T}}({}^{\mathrm{E}}F_r - {}^{\mathrm{E}}F)\\
=&[(\dot{x}_d - \dot{x}) + \Lambda_a(x_d - x) + \Lambda_b(\ddot{x}_d - \ddot{x})\\
&+ \Lambda_c(f_d - f_e)]^{\mathrm{T}}T^{\mathrm{T}}T(f_d - f_e)\\
=&(\dot{x}_d - \dot{x})^{\mathrm{T}}(f_d - f_e) + (x_d - x)^{\mathrm{T}}\Lambda_a^{\mathrm{T}}(f_d - f_e)\\
&+ (\ddot{x}_d - \ddot{x})^{\mathrm{T}}\Lambda_b^{\mathrm{T}}(f_d - f_e) + (f_d - f_e)\Lambda_c^{\mathrm{T}}(f_d - f_e)\\
=&(\dot{x}_d - \dot{x})^{\mathrm{T}}[M_d(\ddot{x} - \ddot{x}_d) + D_d(\dot{x} - \dot{x}_d) + K_d(x - x_d)]\\
&+ (x_d - x)^{\mathrm{T}}\Lambda_a^{\mathrm{T}}[M_d(\ddot{x} - \ddot{x}_d) + D_d(\dot{x} - \dot{x}_d) + K_d(x - x_d)]\\
&+ (\ddot{x}_d - \ddot{x})^{\mathrm{T}}\Lambda_b^{\mathrm{T}}[M_d(\ddot{x} - \ddot{x}_d) + D_d(\dot{x} - \dot{x}_d) + K_d(x - x_d)]\\
&+ [M_d(\ddot{x} - \ddot{x}_d) + D_d(\dot{x} - \dot{x}_d) + K_d(x - x_d)]\Lambda_c^{\mathrm{T}}\\
&[M_d(\ddot{x} - \ddot{x}_d) + D_d(\dot{x} - \dot{x}_d) + K_d(x - x_d)]\\
=&(x_d - x)^{\mathrm{T}}(K_d\Lambda_cK_d - \Lambda_aK_d)(x_d - x) + (\dot{x}_d - \dot{x})^{\mathrm{T}}(D_d\Lambda_cD_d\\
&- D_d)(\dot{x}_d - \dot{x}) + (\ddot{x}_d - \ddot{x})^{\mathrm{T}}(M_d\Lambda_cM_d - \Lambda_bM_d)(\ddot{x}_d - \ddot{x})\\
&+ (\dot{x}_d - \dot{x})^{\mathrm{T}}(2D_d\Lambda_cK_d - \Lambda_aD_d - K_d)(x_d - x)\\
&+ (\dot{x}_d - \dot{x})^{\mathrm{T}}(2D_d\Lambda_cM_d - \Lambda_bD_d - M_d)(\ddot{x}_d - \ddot{x})\\
&+ (x_d - x)^{\mathrm{T}}(2M_d\Lambda_cK_d - \Lambda_bK_d - \Lambda_aM_d)(\ddot{x}_d - \ddot{x}) = 0.\end{aligned} \tag{48}$$

Therefore, the following condition

$$\int_0^\infty p_{\mathrm{E}}\mathrm{d}t \geqslant -\gamma_{\mathrm{E}} \tag{49}$$

holds with $0 \leqslant \gamma_{\mathrm{E}} < \infty$. Then, the compliant object is *virtually stable* according to Definition 4. □

4.2. Virtual Stability of Links

Theorem 2. *Consider the links described by* (2), (4), (5), *combined with their respective control equations* (36), (37), *and with parameter adaptation algorithms, which are the same as* (32) *and* (33) *with appropriate frame substitutions. The links are virtually stable.*

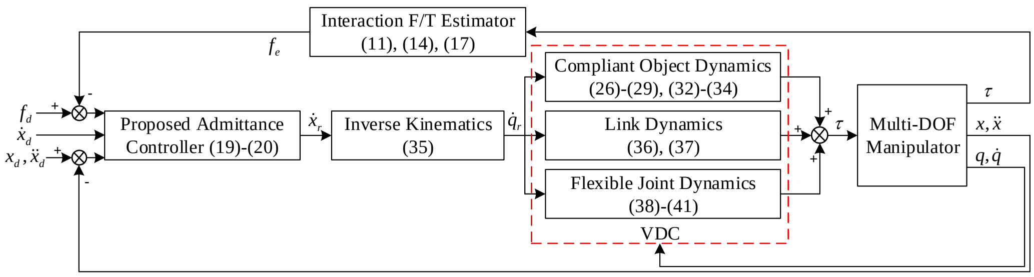

Figure 2: Block diagram of the control system based on VDC.

Proof. Choose the nonnegative accompanying function for the i^{th} link ν_{B_i} as

$$\begin{aligned}\nu_{\mathrm{B}_i} =&\frac{1}{2}({}^{\mathrm{B}_i}V_r - {}^{\mathrm{B}_i}V)^{\mathrm{T}} M_{\mathrm{B}_i}({}^{\mathrm{B}_i}V_r - {}^{\mathrm{B}_i}V)\\ &+\frac{1}{2}\sum_{\gamma=1}^{13}\frac{(\theta_{\mathrm{B}_i\gamma}-\hat{\theta}_{\mathrm{B}_i\gamma})^2}{\rho_{\mathrm{B}_i\gamma}},\end{aligned} \tag{50}$$

then, the time derivative of (50) can be obtained as

$$\begin{aligned}\dot{\nu}_{\mathrm{B}_i} \leqslant& -({}^{\mathrm{B}_i}V_r - {}^{\mathrm{B}_i}V)^{\mathrm{T}} K_{\mathrm{B}_i}({}^{\mathrm{B}_i}V_r - {}^{\mathrm{B}_i}V)\\ &+({}^{\mathrm{B}_i}V_r - {}^{\mathrm{B}_i}V)^{\mathrm{T}}({}^{\mathrm{B}_i}F_r^* - {}^{\mathrm{B}_i}F^*).\end{aligned} \tag{51}$$

In view of (5), (37), and Definition 3, it yields

$$\begin{aligned}&({}^{\mathrm{B}_n}V_r - {}^{\mathrm{B}_n}V)^{\mathrm{T}}({}^{\mathrm{B}_n}F_r^* - {}^{\mathrm{B}_n}F^*)\\ &= ({}^{\mathrm{B}_n}V_r - {}^{\mathrm{B}_n}V)^{\mathrm{T}}[({}^{\mathrm{B}_n}F_r - {}^{\mathrm{B}_n}F) - {}^{\mathrm{B}_n}U_{\mathrm{T_O}}({}^{\mathrm{T_O}}F_r - {}^{\mathrm{T_O}}F)]\\ &= p_{\mathrm{B}_n} - [{}^{\mathrm{B}_n}U_{\mathrm{T_O}}^{\mathrm{T}}({}^{\mathrm{B}_n}V_r - {}^{\mathrm{B}_n}V)]^{\mathrm{T}}({}^{\mathrm{T_O}}F_r - {}^{\mathrm{T_O}}F)\\ &= p_{\mathrm{B}_n} - p_{\mathrm{T_O}},\end{aligned} \tag{52}$$

$$\begin{aligned}&({}^{\mathrm{B}_i}V_r - {}^{\mathrm{B}_i}V)^{\mathrm{T}}({}^{\mathrm{B}_i}F_r^* - {}^{\mathrm{B}_i}F^*)\\ &= ({}^{\mathrm{B}_i}V_r - {}^{\mathrm{B}_i}V)^{\mathrm{T}}[({}^{\mathrm{B}_i}F_r - {}^{\mathrm{B}_i}F) - {}^{\mathrm{B}_i}U_{\mathrm{T}_{i+1}}({}^{\mathrm{T}_{i+1}}F_r - {}^{\mathrm{T}_{i+1}}F)]\\ &= p_{\mathrm{B}_i} - [{}^{\mathrm{B}_i}U_{\mathrm{T}_{i+1}}^{\mathrm{T}}({}^{\mathrm{B}_i}V_r - {}^{\mathrm{B}_i}V)]^{\mathrm{T}}({}^{\mathrm{T}_{i+1}}F_r - {}^{\mathrm{T}_{i+1}}F)\\ &= p_{\mathrm{B}_i} - p_{\mathrm{T}_{i+1}}, \quad i = 1, \ldots, n-1.\end{aligned} \tag{53}$$

As shown in Fig. 1, each link has two cutting points, one driving cutting point associated with frame $\{\mathrm{T}_{i+1}\}, i \in [1, n-1]$ or associated with frame $\{\mathrm{T_O}\}, i = n$, and one driven cutting point associated with frame $\{\mathrm{B}_i\}, i \in [1, n]$. Therefore, all the links are *virtually stable* in the sense of Definition 4. □

4.3. Virtual Stability of Joints

Theorem 3. *Consider the flexible joints described by* (6), (7), (8)*, combined with their respective control equations* (38), (39)*, and with the parameter adaptation algorithms* (40) *and* (41)*. The flexible joints are virtually stable.*

Proof. Select the nonnegative accompanying function for the i^{th} joint as

$$\begin{aligned}\nu_{fi} =&\frac{1}{2}I_{mi}(\dot{\phi}_{ir}-\dot{\phi}_i)^2 + \frac{1}{2}\sum_{\gamma=1}^{2}\frac{(\theta_{ai\gamma}-\hat{\theta}_{ai\gamma})^2}{\rho_{ai\gamma}}+\\ &\frac{1}{2}\sum_{i=\gamma}^{3}\frac{(\theta_{bi\gamma}-\hat{\theta}_{bi\gamma})^2}{\rho_{bi\gamma}},\end{aligned} \tag{54}$$

then, combined with the third equations of (6) and (38), the time derivative of ν_{fi} defined by (54) can be expressed as

$$\begin{aligned}\dot{\nu}_{fi} \leqslant& -k_{vqi}(\dot{q}_{ir}-\dot{q}_i)^2 - k_{v\phi i}(\dot{\phi}_{ir}-\dot{\phi}_i)^2 + (\dot{q}_{ir}-\dot{q}_i)(\tau_{tid}-\tau_{ti})\\ &-(\dot{\phi}_{ir}-\dot{\phi}_i)(\tau_{tid}-\tau_{ti}) - (\dot{q}_{ir}-\dot{q}_i)z^{\mathrm{T}}({}^{\mathrm{B}_i}F_r - {}^{\mathrm{B}_i}F).\end{aligned} \tag{55}$$

Subtracting the second equation of (6) from the second equation of (38) yields

$$\begin{aligned}\tau_{tid} - \tau_{ti} =&\hat{k}_{fi}(\phi_{ir}-q_{ir}) - k_{fi}(\phi_i - q_i)\\ =& -(k_{fi}-\hat{k}_{fi})(\phi_{ir}-q_{ir})+\\ &k_{fi}[(\phi_{ir}-\phi_i)-(q_{ir}-q_i)],\end{aligned} \tag{56}$$

then, substituting (56) into (55) and employing the third equation of (40) derives

$$\begin{aligned}\dot{\nu}_{fi} \leqslant& -k_{vqi}(\dot{q}_{ir}-\dot{q}_i)^2 - k_{v\phi i}(\dot{\phi}_{ir}-\dot{\phi}_i)^2 + [(\dot{\phi}_{ir}-\dot{\phi}_i)-\\ &(\dot{q}_{ir}-\dot{q}_i)]\Big\{(k_{fi}-\hat{k}_{fi})(\phi_{ir}-q_{ir}) - k_{fi}[(\phi_{ir}-\phi_i)-\\ &(q_{ir}-q_i)]\Big\} - (\dot{q}_{ir}-\dot{q}_i)z^{\mathrm{T}}({}^{\mathrm{B}_i}F_r - {}^{\mathrm{B}_i}F)\\ =& -k_{vqi}(\dot{q}_{ir}-\dot{q}_i)^2 - k_{v\phi i}(\dot{\phi}_{ir}-\dot{\phi}_i)^2 - k_{fi}[(\dot{\phi}_{ir}-\dot{\phi}_i)-\\ &(\dot{q}_{ir}-\dot{q}_i)][(\phi_{ir}-\phi_i)-(q_{ir}-q_i)] + (k_{fi}-\hat{k}_{fi})s_{kfi}-\\ &(\dot{q}_{ir}-\dot{q}_i)z^{\mathrm{T}}({}^{\mathrm{B}_i}F_r - {}^{\mathrm{B}_i}F).\end{aligned} \tag{57}$$

According to the third equation of (41) and Definition 2, we can obtain

$$(k_{fi}-\hat{k}_{fi})\Big(s_{kfi} - \dot{\hat{k}}_{fi}/\rho_{kfi}\Big) \leqslant 0. \tag{58}$$

Finally, choose the nonnegative accompanying function for the i^{th} joint with joint elasticity considered as

$$\nu_{ai} = \nu_{fi} + \frac{1}{2}k_{fi}[(\phi_{ir}-\phi_i)-(q_{ir}-q_i)]^2 + \frac{1}{2}(k_{fi}-\hat{k}_{fi})^2/\rho_{kfi}, \tag{59}$$

where ν_{fi} is defined in (54). Then, it follows from (57) and (58) that

$$\dot{\nu}_{ai} \leqslant -k_{vqi}(\dot{q}_{ir}-\dot{q}_i)^2 - k_{v\phi i}(\dot{\phi}_{ir}-\dot{\phi}_i)^2 - (\dot{q}_{ir}-\dot{q}_i)z^{\mathrm{T}}({}^{\mathrm{B}_i}F_r - {}^{\mathrm{B}_i}F) \tag{60}$$

holds.

According to (2), (5), (36), (37), and Definition 3, we can derive

$$\begin{aligned}&\dot{\nu}_{a1} \leqslant -k_{vq1}(\dot{q}_{1r}-\dot{q}_1)^2 - k_{v\phi 1}(\dot{\phi}_{1r}-\dot{\phi}_1)^2 - p_{\mathrm{B}_1},\\ &\dot{\nu}_{ai} \leqslant -k_{vqi}(\dot{q}_{ir}-\dot{q}_i)^2 - k_{v\phi i}(\dot{\phi}_{ir}-\dot{\phi}_i)^2 - p_{\mathrm{B}_i} + p_{\mathrm{T}_i}, i \in [2, n].\end{aligned} \tag{61}$$

As shown in Fig. 1, joint 1 only has one driving cutting point associated with frame $\{B_1\}$. Joint $i, i \in [2, n]$ has two cutting points, one driving cutting point associated with frame $\{B_i\}$ and one driven cutting point associated with frame $\{T_i\}$. Therefore, all the flexible joints are *virtually stable* in the sense of Definition 4. □

4.4. Stability of Multi-DOF Manipulator System

The following lemmas in Zhu (2010) are used to prove the L_2 and L_∞ stability of the entire robotic system.

Lemma 1. *Consider a non-negative piecewise continuous function $\xi(t)$ described as*

$$\xi(t) \geqslant \frac{1}{2} x^{\mathrm{T}}(t) P x(t), \tag{62}$$

where $x(t) \in \mathbb{R}^n$, $n \geqslant 1$, and $P \in \mathbb{R}^{n\times n}$ is a symmetric positive-definite matrix. If the derivative of $\xi(t)$ with respect to time is Lebesgue integrable and subject to

$$\dot{\xi}(t) \leqslant -y^{\mathrm{T}}(t) Q y(t) - s(t) \tag{63}$$

with $y(t) \in \mathbb{R}^m$, $m \geqslant 1$, and $Q \in \mathbb{R}^{m\times m}$ being a symmetric positive-definite matrix, and $s(t)$ is governed by

$$\int_0^\infty s(t) dt \geqslant -\gamma_0 \tag{64}$$

with $0 \leqslant \gamma_0 < \infty$, then it follows that $\xi(t) \in L_\infty$, $x(t) \in L_\infty$, and $y(t) \in L_2$ hold.

Lemma 2. *Consider a multiple-input-multiple-output second-order system described by*

$$M\ddot{x}(t) + D\dot{x}(t) + Kx(t) = u(t) \tag{65}$$

with $x(t) \in \mathbb{R}^n$, $u(t) \in \mathbb{R}^n$. $M \in \mathbb{R}^{n\times n}$, $D \in \mathbb{R}^{n\times n}$, and $K \in \mathbb{R}^{n\times n}$ being symmetrical and positive definite. If $u(t) \in L_2 \cap L_\infty$, then $x(t) \in L_2 \cap L_\infty$ and $\dot{x}(t) \in L_2 \cap L_\infty$.

Lemma 3. *If $e(t) \in L_2$ and $\dot{e}(t) \in L_\infty$, then $\lim_{t\to\infty} e(t) = 0$.*

Lemma 3 is of great importance in proving the asymptotic convergence for an error signal $e(t)$.

Theorem 4. *Consider the manipulator, shown in Fig. 3 and described by* (48)*. Furthermore, let the conclusions in* (47)*,* (51)*, and* (61) *hold. The stability of the manipulator can be guaranteed.*

Proof. Define the nonnegative accompanying function for the entire system as

$$\nu = \nu_{\mathrm{O}} + \sum_{i=1}^{n} \nu_{\mathrm{B}_i} + \sum_{i=1}^{n} \nu_{ai}, \tag{66}$$

and according to (47), (48), (51), and (61), the time derivative of (66) can be derived as

$$\begin{aligned} \dot{\nu} \leqslant & -({}^{\mathrm{O}}V_r - {}^{\mathrm{O}}V)^{\mathrm{T}} K_{\mathrm{O}} ({}^{\mathrm{O}}V_r - {}^{\mathrm{O}}V) \\ & - \sum_{i=1}^{n} ({}^{\mathrm{B}_i}V_r - {}^{\mathrm{B}_i}V)^{\mathrm{T}} K_{\mathrm{B}_i} ({}^{\mathrm{B}_i}V_r - {}^{\mathrm{B}_i}V) \\ & - \sum_{i=1}^{n} \left[k_{vqi} (\dot{q}_{ir} - \dot{q}_i)^2 + k_{v\phi i} (\dot{\phi}_{ir} - \dot{\phi}_i)^2 \right]. \end{aligned} \tag{67}$$

Then, integrating (67) over time from $t = 0$ to $t = T$, $\forall T > 0$ obtains

$$\int_0^T (\dot{q}_{ir} - \dot{q}_i)^2 dt \leqslant \frac{1}{k_{vqi}} \nu(0), \tag{68}$$

$$\int_0^T (\dot{\phi}_{ir} - \dot{\phi}_i)^2 dt \leqslant \frac{1}{k_{\phi qi}} \nu(0). \tag{69}$$

Combining Lemma 1, (66), and (67) yields

$$\begin{aligned} {}^{\mathrm{O}}V_r - {}^{\mathrm{O}}V &\in L_2 \cap L_\infty, \\ {}^{\mathrm{B}_i}V_r - {}^{\mathrm{B}_i}V &\in L_2 \cap L_\infty, \\ (\phi_{ir} - \phi_i) - (q_{ir} - q_i) &\in L_\infty. \end{aligned} \tag{70}$$

It further follows from (2), (36), (68), (69), and (70) that

$$\begin{aligned} \dot{q}_{ir} - \dot{q}_i &\in L_2 \cap L_\infty, \\ \dot{\phi}_{ir} - \dot{\phi}_i &\in L_2 \cap L_\infty. \end{aligned} \tag{71}$$

According to (2), (24), (26), (27), and (70), it obtains

$$\dot{x}_r - \dot{x} \in L_2 \cap L_\infty. \tag{72}$$

Then, it yields

$$\begin{aligned} & \Lambda_c^{-1} (\dot{x}_d - \dot{x}) + \Lambda_c^{-1} \Lambda_a (x_d - x) \\ & + \Lambda_c^{-1} \Lambda_b (\ddot{x}_d - \ddot{x}) + (f_d - f_e) \in L_2 \cap L_\infty \end{aligned} \tag{73}$$

using (19). □

When $(f_d - f_e) = 0$, it follows from Lemma 2 that $(\dot{x}_d - \dot{x}) \in L_2 \cap L_\infty$ and $(x_d - x) \in L_2 \cap L_\infty$. Then, according to Lemma 3, $\lim_{t\to\infty} (x_d(t) - x(t)) = 0$.

It is worth mentioning that $(f_d - f_e) \neq 0$ denotes constrained motions and $(f_d - f_e) = 0$, with $f_d = [0, 0, 0]^{\mathrm{T}}$, denotes free-space motions.

5. Experimental Results

Several experiments were conducted to verify the efficiency of the proposed approach for multi-DOF manipulator control. The experimental setup is introduced in Section 5.1. Section 5.2 provides the experimental verification of the generalized momentum-based force estimation approach and the proposed admittance control based on the low-level VDC. Section 5.3 demonstrates the performance of the proposed approach in handling compliant motion/force operation.

5.1. Experimental Setup

The experimental setup is shown in Fig. 3, which consists of a 7-DOF manipulator Kinova Gen3 (Kinova Robotics, Canada) and an Axia80-ZC22 F/T sensor (ATI Industrial Automation, Apex, NC, USA). The Gen3 employs series elastic elements to sense joint torques. It should be noted that the proposed method is also applicable to other types of multi-DOF manipulators with joint torque available, such as Kuka LBR iiwa (Mujica et al., 2020) or Franka Emika Panda (Gaz et al., 2019). The control frequency of the system is set as 1000 Hz (1.0 ms per

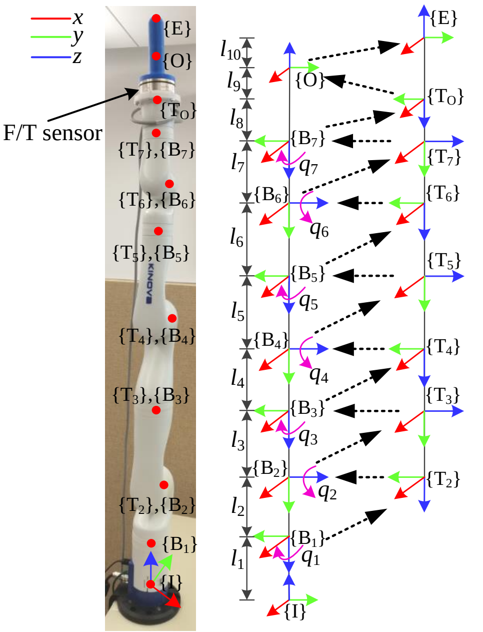

Figure 3: Virtual decomposition of the tested manipulator.

loop). It is worth mentioning that the end-effector in Fig. 3 is considered as the object to facilitate the controller design of the subsystem dynamics. The F/T sensor is mostly used to evaluate the accuracy of the force estimation approach rather than as a control component.

Manipulator torque compensation is first conducted to estimate the interaction force. The joint friction model is shown in (8). The manipulator's dynamics and gravity-related parameters are provided by Kinova Robotics, and the joint friction parameters are estimated via a least-square method[2] (Calanca et al., 2010). It is noteworthy that these estimated joint friction parameters are not the ones in (38). These are fixed parameters used for interaction force estimation, and the parameters in (38) are adaptive ones for control purposes. The joint stiffness coefficients in (6) are obtained from Kinova Robotics, which are listed as $k_f = [16, 16, 16, 16, 7.1, 7.1, 7.1]^{\mathrm{T}}$kN·m/rad. The task-space acceleration is obtained by differentiating the task-space velocity. A fourth-order Butterworth low-pass filter is performed on the acceleration and the measured joint torque to mitigate the measurement noise effect, with the cutoff frequency of 5 Hz and 3 Hz, respectively.

A video is attached with the manuscript to present the experiments in this section.

5.2. Admittance Control Based on VDC

In this experiment, the proposed method's performance in following a task-space trajectory, which is generated by a human-applied F/T at the end-effector via a VDC-based admittance controller, is verified. First, we employed a PD controller on the end-effector's orientation to keep it constant; thus, only position compliance was involved. Second, a similar required angular velocity definition as (19) was utilized on the orientation to prove the method's effectiveness for orientation compliance, where the desired/actual force (f_d/f_e) should be replaced by the desired/actual torque (τ_d/τ_e). This trick allowed the influences of forces and torques to be separated; the results were, therefore, more accurate.

Table 1: Desired admittance parameters and control gains.

	x transl.	y transl.	z transl.	x rot.
K_d	0	0	0	0
D_d	250	250	125	1.5
M_d	25	25	12.5	0.15
Λ_a	0	0	0	0
Λ_b	0.1	0.1	0.1	0.1
Λ_c	0.004	0.004	0.008	2/3

The subsequent experiments consist of two segments. The first one proves the precision of the generalized momentum-based interaction F/T estimation approach. The estimated F/T (computed via (11), (14), and (17)) is compared with the F/T measured by the wrist sensor.

The desired F/T f_d/τ_d and trajectory x_d were set as zero. It is noteworthy that for orientation compliance, the rotation around the base frame's x-axis was taken as an example. The desired admittance parameters and control gains are listed in Table 1. The units of K_d, D_d, and M_d for translation are N/m, Ns/m, and Ns^2/m. The units of K_d, D_d, and M_d for rotation are N/(m·rad), Ns/(m·rad), and Ns^2/(m·rad). The stiffness of the manipulator was zero to let the end-effector follow the trajectory generated only by the user-applied F/T. In terms of translation, the damping and inertial values of the z-axis were smaller than those of the other two directions to test the effectiveness of realizing different admittance behaviors in different directions. The control gains were selected according to the desired admittance parameters and (20).

Fig. 4 presents the end-effector's translation results with fixed orientation. Fig. 5 shows its x-axis rotation results, where the translation setting was the same as the pure translation scenario, but the user did not apply any force. Table 2 contains the maximum and RMS values of the estimation errors in each direction. During the translation experiment, the operator first applied the force in x-axis, then, in y-axis, and finally in z-axis. As shown in Fig. 4 and the first three columns of Table 2, the maximum task-space force estimation errors between the estimated forces and the force measurements in x, y, and z were 5.53 N, 5.84 N, and 4.12 N, respectively. The RMS level of these estimation errors was 1.30 N, 1.40 N, and 1.18 N, respectively, which accounted for about 5.27%, 7.22%, and 9.25% of their corresponding maximum force measurements. The x-axis torque estimation result is presented in Fig. 5 and the last column of Table 2, where the maximum and RMS estimation errors occupied 17.94% and 5.60% of its maximum

[2] The parameter identification experiment is performed by controlling the manipulator to track predefined task-space trajectories via PID controller with joint position, velocity, and torque recorded.

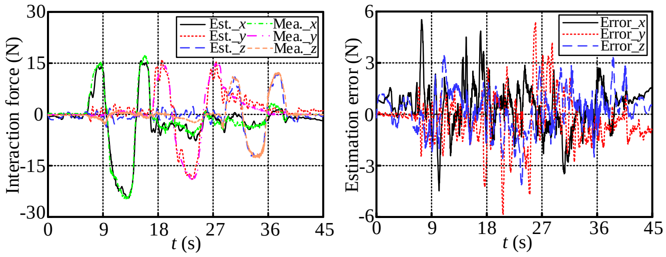

(a) Interaction force (b) Estimation error

Figure 4: Comparison of estimated force and measured force.

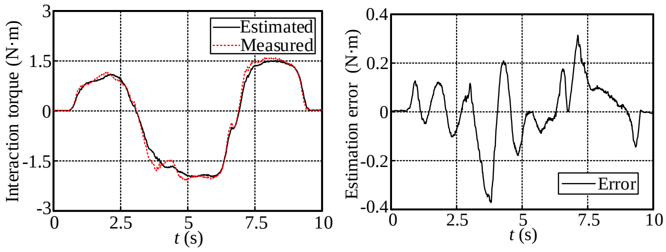

(a) Interaction torque (b) Estimation error

Figure 5: Comparison of estimated torque and measured torque in x-axis.

torque measurement, respectively. The experimental results in this segment verify the effectiveness of the interaction force estimation method.

The second segment is to illustrate the performance of the admittance controller based on the low-level VDC in terms of trajectory following exerted by an arbitrary external F/T. The control gains were selected the same as the first experiment segment. Fig. 6 shows some pictures during the experiment, indicating that the trajectory following can be achieved in each Cartesian direction with the corresponding estimated interaction F/T. However, each direction's admittance behavior was different due to the different control gains. Fig. 7 shows the end-effector's position and force profiles during the translation experiment. Its orientation compliance result around the x-axis is provided in Fig. 8.

Fig. 7a shows the task-space displacements of the end-effector during the translation experiment, the displacements along x, y, and z occurred sequentially due to the external forces. Fig. 8a presents the end-effector's x-axis orientation induced by a user-applied torque. Figs. 7b and 8b show the estimated and fitted forces and torques during the two experiments, respectively. The fitted forces/torques were calculated according to (18) and the desired admittance parameters from Table 1. The RMS values of the estimated and fitted force differences in x, y, and z were 1.74 N, 1.19 N, and

Table 2: Maximum and RMS values of F/T estimation errors.

	x transl.	y transl.	z transl.	x rot.
Max. error	5.53 N	5.84 N	4.12 N	0.37 N·m
RMS error	1.30 N	1.40 N	1.18 N	0.12 N·m

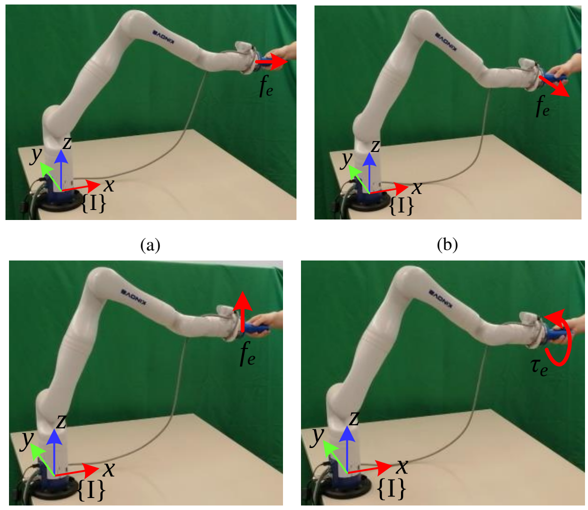

Figure 6: Pictures of trajectory following experiment. (a) shows the translation along x, (b) shows the translation along y, (c) shows the translation along z, and (d) shows the rotation around x.

0.73 N, respectively. The RMS value of the estimated and fitted x-axis torque difference was 0.088 N·m. The nearly perfect matching of the estimated and fitted results indicates the proposed approach's effectiveness in following a random trajectory generated by manual F/T.

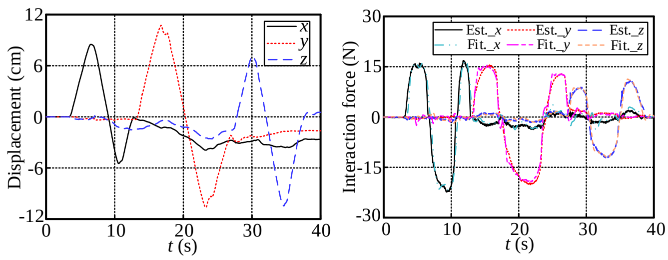

(a) Task-space displacement (b) Interaction force

Figure 7: Experimental results with trajectory following generated by manual force.

5.3. *Compliant Motion/Force Operation*

This experiment evaluates the controller's capability to perform the desired admittance behavior in both free-space and constrained space. The end-effector's orientation was maintained using a simple PD controller. A desired trajectory in the $y - z$ plane of the base frame was provided for the end-effector with its definition being $x_d(t) = x_0 + [0, 0.1\sin(\pi/5t), 0.08\sin(2\pi/5t)]^{\mathrm{T}}$ m, where x_0 represented the end-effector's initial position. However, an obstacle prevented its motion in z when contact occurred. The control parameters of this experiment were set as $\Lambda_a = \mathrm{diag}(15, 15, 6)$, $\Lambda_b = \mathrm{diag}(0.2, 0.2, 0.2)$, $\Lambda_c = \mathrm{diag}(0.001, 0.001, 0.005)$, the desired force was defined as 0 N. This parameter design made the system stiff along x and y, and compliant along z.

Here, we compared two scenarios to demonstrate the effectiveness of the proposed method. One was to employ the

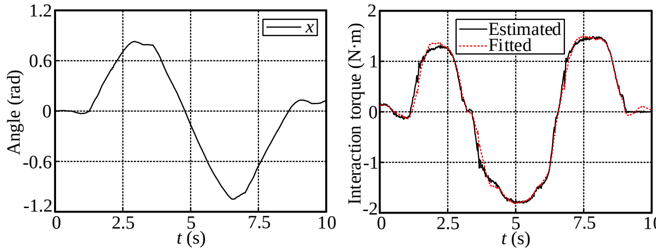

(a) x-axis orientation (b) Interaction torque

Figure 8: Experimental results with orientation tracking generated by manual torque.

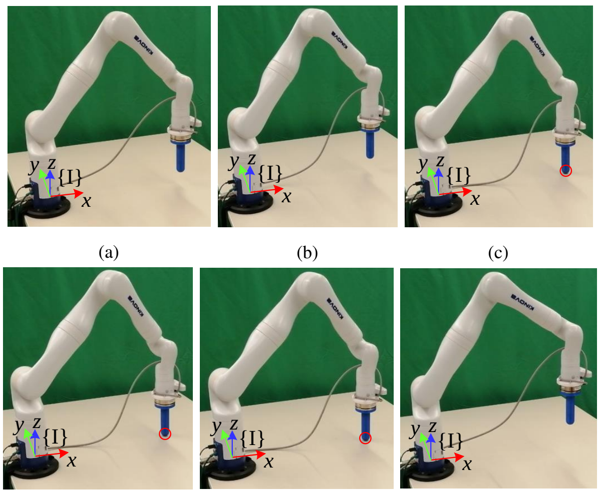

(a) (b) (c)

(d) (e) (f)

Figure 9: Pictures of compliant motion/force operation. (a) shows the initial pose of the manipulator, (b) shows the free-space motion, (c) shows the critical point between the free-space and constrained motions, (d) shows the constrained space motion, (e) shows the critical point between the constrained space and free-space motions, and (f) shows the free-space motion.

estimated task-space force, and the other was to implement the measured interaction force. Some pictures of the experiment are shown in Fig. 9, where the red circle denotes the contact point during the constrained motion.

The experimental results are shown in Figs. 10 and 11, where Fig. 10 presents the results with the measured interaction force and Fig. 11 provides the results with the estimated force. In the two figures, the left subgraph shows the desired and actual task-space trajectories, the upper right subgraph shows the trajectory tracking error in y, and the lower right subgraph shows the measured/estimated contact forces in z. Here, the period of the task-space motion was 10 s, and two periods were recorded. Because the desired trajectory was defined in the $y - z$ plane, only the results in that plane were presented. It is evident that in both two scenarios, when contact occurred in z direction, the proposed VDC-based admittance controller could automatically adjust its trajectory command to avoid tremendous contact force. Take time of 3.57 s with experiment using measured force for example, where the minimum desired and actual end-effector's positions in z were 15.87 cm and 18.42 cm, respectively. Then, the maximum interaction force

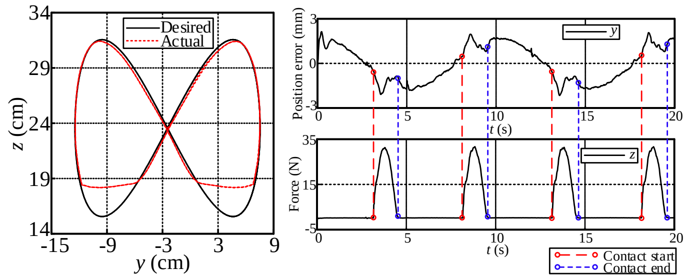

Figure 10: Experimental results of compliant motion/force operation with measured force.

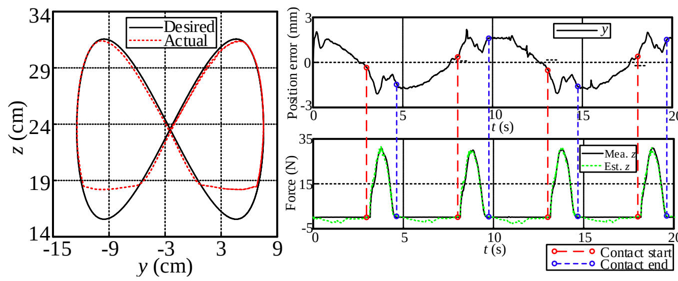

Figure 11: Experimental results of compliant motion/force operation with estimated force.

could be estimated according to (18) as $f_e \approx f_d - K_d(x - x_d) = 0 - 1200 \times (0.1587 - 0.1842) = 30.60$ N, which was consistent with the lower right subgraph of Fig. 10. In contrast, the trajectory tracking accuracy in y direction was still desirable, with maximal tracking error less than 2.5 mm.

To evaluate the precision of the proposed method in achieving the desired task-space compliance, the position/force data obtained in the constrained motion (18.22 s – 19.38 s in Fig. 10 and 18.14 s – 19.46 s in Fig. 11) was used to estimate the actual admittance parameters in z via a least-square method. Table 3 lists the estimation results. In the experiment with the estimated force, the measured force was employed to calculate the actual admittance parameters to illustrate the comparable performance with/without an F/T sensor.

The estimation errors using the measured force for M_d, D_d, and K_d were 7.4 Ns^2/m, 12.4 Ns/m, and 28.8 N/m, accounting for about 18.50%, 6.20%, and 2.40% of the desired parameters, respectively. While their values using the estimated force for M_d, D_d, and K_d were 14.5 Ns^2/m, 19.8 Ns/m, and 88.6 N/m, accounting for about 36.25%, 9.90%, and 7.38% of the desired parameters, respectively. The estimation error for M_d was a little large because the task-space acceleration was derived via

Table 3: Desired and actual admittance parameters.

	M_d (Ns^2/m)	D_d (Ns/m)	K_d (N/m)
Desired	40	200	1200
Actual (measured)	47.4	187.6	1228.8
Actual (estimated)	54.5	180.2	1288.6

the derivative of velocity, which introduced some measurement errors. However, the parameter estimation accuracy of D_d and K_d was rather high. The similar parameter estimation results confirm the feasibility of using the estimated force to realize compliant motion/force operation.

6. Conclusions

This paper proposes a novel virtual decomposition control (VDC)-based admittance control approach of multi-DOF manipulators considering joint flexibility using hierarchical design framework. The high-level admittance controller is executed based on the low-level VDC. The interaction force/torque (F/T) is obtained using a generalized momentum-based force estimation method. The admittance controller with a low-level VDC control loop can improve a multi-DOF manipulator's bandwidth and handle robot-environment interaction simultaneously. Moreover, a VDC-based adaptive controller is proposed for joint friction, flexibility, etc., to further improve the system's control accuracy. The L_2 and L_∞ stability of the VDC-based admittance controller is guaranteed for both free-space and constrained motions, and the asymptotic convergence of the end-effector's trajectory tracking has been proved for free-space movement.

The proposed approach's effectiveness was experimentally verified. The accuracy of the generalized momentum-based force estimation method for both task-space force and torque was desirable. The RMS level of the estimation errors was no more than 10% of their maximum measurements. For the VDC-based admittance controller, the maximum estimation error ratios of the desired admittance parameters K_d, D_d, and M_d were 7.38%, 9.90%, and 36.25%, respectively, when the estimated interaction force was employed.

In future work, we will consider controlling a wheeled mobile manipulator system to enlarge the system's workspace. Also, bilateral teleoperation will be taken into account, where the robotic system can be haptically teleoperated from one or two user interfaces.

Acknowledgements

This work was supported by Canada Foundation for Innovation (CFI), the Natural Sciences and Engineering Research Council (NSERC) of Canada, the Canadian Institutes of Health Research (CIHR), the Alberta Advanced Education Ministry, the Alberta Economic Development, Trade and Tourism Ministry's grant to Centre for Autonomous Systems in Strengthening Future Communities, the National Natural Science Foundation of China (Grant No. 91948202, 51822502), the "111" Project (Grant No. B07018), and the China Scholarship Council under Grant [2019]06120165.

References

Antonelli, G., Caccavale, F., Chiaverini, S., 2004. Adaptive tracking control of underwater vehicle-manipulator systems based on the virtual decomposition approach. IEEE Transactions on Robotics and Automation 20, 594–602.

Asl, H.J., Katagiri, K., Narikiyo, T., Yamashita, M., Kawanishi, M., 2021. Augmenting human power by assistive robots: Application of adaptive neural networks. Control Engineering Practice 110, 104769.

Buondonno, G., De Luca, A., 2015. A recursive Newton-Euler algorithm for robots with elastic joints and its application to control, in: IEEE/RSJ International Conference on Intelligent Robots and Systems, pp. 5526–5532.

Calanca, A., Capisani, L.M., Ferrara, A., Magnani, L., 2010. MIMO closed loop identification of an industrial robot. IEEE Transactions on Control Systems Technology 19, 1214–1224.

Carriere, J., Fong, J., Meyer, T., Sloboda, R., Husain, S., Usmani, N., Tavakoli, M., 2019. An admittance-controlled robotic assistant for semi-autonomous breast ultrasound scanning, in: 2019 International Symposium on Medical Robotics (ISMR), IEEE. pp. 1–7.

Chen, J., Ro, P.I., 2022. Human intention-oriented variable admittance control with power envelope regulation in physical human-robot interaction. Mechatronics 84, 102802.

De Luca, A., Albu-Schaffer, A., Haddadin, S., Hirzinger, G., 2006. Collision detection and safe reaction with the DLR-III lightweight manipulator arm, in: IEEE/RSJ International Conference on Intelligent Robots and Systems, pp. 1623–1630.

Du, Q., Song, C., Ding, W., Zhao, L., Luo, Y., 2021. Vibration suppression method of humanoid flexible arm based on model-free predictive control. Advanced Robotics 35, 450–458.

Fateh, M.M., 2012. Robust control of flexible-joint robots using voltage control strategy. Nonlinear Dynamics 67, 1525–1537.

Ficuciello, F., Romano, A., Villani, L., Siciliano, B., 2014. Cartesian impedance control of redundant manipulators for human-robot co-manipulation, in: IEEE/RSJ International Conference on Intelligent Robots and Systems, pp. 2120–2125.

Ficuciello, F., Villani, L., Siciliano, B., 2015. Variable impedance control of redundant manipulators for intuitive human–robot physical interaction. IEEE Transactions on Robotics 31, 850–863.

Gaz, C., Cognetti, M., Oliva, A., Giordano, P.R., De Luca, A., 2019. Dynamic identification of the franka emika panda robot with retrieval of feasible parameters using penalty-based optimization. IEEE Robotics and Automation Letters 4, 4147–4154.

Ghorbel, F., Hung, J., Spong, M., 1989. Adaptive control of flexible-joint manipulators. IEEE Control Systems Magazine 9, 9–13.

Han, L., Xu, W., Li, B., Kang, P., 2019. Collision detection and coordinated compliance control for a dual-arm robot without force/torque sensing based on momentum observer. IEEE/ASME Transactions on Mechatronics 24, 2261–2272.

Hogan, N., 1985. Impedance control: An approach to manipulation: Parts I-III. Journal of Dynamic System, Measurement, and Control 107, 1–24.

Hollerbach, J.M., 1980. A recursive lagrangian formulation of maniputator dynamics and a comparative study of dynamics formulation complexity. IEEE Transactions on Systems, Man, and Cybernetics 10, 730–736.

Jafarinasab, M., Sirouspour, S., Dyer, E., 2019. Model-based motion control of a robotic manipulator with a flying multirotor base. IEEE/ASME Transactions on Mechatronics 24, 2328–2340.

Karayiannidis, Y., Smith, C., Barrientos, F.E.V., Ögren, P., Kragic, D., 2016. An adaptive control approach for opening doors and drawers under uncertainties. IEEE Transactions on Robotics 32, 161–175.

Kim, M.J., Beck, F., Ott, C., Albu-Schäffer, A., 2019. Model-free friction observers for flexible joint robots with torque measurements. IEEE Transactions on Robotics 35, 1508–1515.

Koivumäki, J., Zhu, W.H., Mattila, J., 2019. Energy-efficient and high-precision control of hydraulic robots. Control Engineering Practice 85, 176–193.

Koivumäki, J., Mattila, J., 2017. Stability-guaranteed impedance control of hydraulic robotic manipulators. IEEE/ASME Transactions on Mechatronics 22, 601–612.

Liu, X., Zhao, F., Ge, S.S., Wu, Y., Mei, X., 2019. End-effector force estimation for flexible-joint robots with global friction approximation using neural networks. IEEE Transactions on Industrial Informatics 15, 1730–1741.

Luna, C.O., Rahman, M.H., Saad, M., Archambault, P., Zhu, W.H., 2016. Virtual decomposition control of an exoskeleton robot arm. Robotica 34, 1587–1609.

Ma, H., Zhou, Q., Li, H., Lu, R., 2021. Adaptive prescribed performance control of a flexible-joint robotic manipulator with dynamic uncertainties. IEEE Transactions on Cybernetics , 1–11.

Madsen, E., Rosenlund, O.S., Brandt, D., Zhang, X., 2020. Comprehensive modeling and identification of nonlinear joint dynamics for collaborative industrial robot manipulators. Control Engineering Practice 101, 104462.

Mai, T., Wang, Y., 2014. Adaptive force/motion control system based on recurrent fuzzy wavelet cmac neural networks for condenser cleaning crawler-type mobile manipulator robot. IEEE Transactions on Control Systems Technology 22, 1973–1982.

Mohammadi, A., Tavakoli, M., Marquez, H.J., Hashemzadeh, F., 2013. Nonlinear disturbance observer design for robotic manipulators. Control Engineering Practice 21, 253–267.

Mujica, M., Benoussaad, M., Fourquet, J.Y., 2020. Evaluation of human-robot object co-manipulation under robot impedance control, in: IEEE International Conference on Robotics and Automation, pp. 9143–9149.

Ochoa Luna, C., Habibur Rahman, M., Saad, M., Archambault, P.S., Bruce Ferrer, S., 2015. Admittance-based upper limb robotic active and active-assistive movements. International Journal of Advanced Robotic Systems 12, 117.

Ott, C., Mukherjee, R., Nakamura, Y., 2010. Unified impedance and admittance control, in: IEEE International Conference on Robotics and Automation, pp. 554–561.

Raibert, M.H., Craig, J.J., 1981. Hybrid Position/Force Control of Manipulators. Journal of Dynamic Systems, Measurement, and Control 103, 126–133.

Ren, T., Dong, Y., Wu, D., Chen, K., 2018. Collision detection and identification for robot manipulators based on extended state observer. Control Engineering Practice 79, 144–153.

Sciavicco, L., Siciliano, B., 2012. Modelling and control of robot manipulators. Springer Science & Business Media.

Sharifi, M., Behzadipour, S., Salarieh, H., Tavakoli, M., 2020. Assist-as-needed policy for movement therapy using telerobotics-mediated therapist supervision. Control Engineering Practice 101, 104481.

Siciliano, B., Sciavicco, L., Villani, L., Oriolo, G., 2010. Robotics: modelling, planning and control. Springer Science & Business Media.

Spong, M.W., 1987. Modeling and control of elastic joint robots. Journal of Dynamic Systems, Measurement, and Control 109, 310–319.

Torabi, A., Khadem, M., Zareinia, K., Sutherland, G.R., Tavakoli, M., 2019. Application of a redundant haptic interface in enhancing soft-tissue stiffness discrimination. IEEE Robotics and Automation Letters 4, 1037–1044.

Wang, H., 2016. Adaptive control of robot manipulators with uncertain kinematics and dynamics. IEEE Transactions on Automatic Control 62, 948–954.

Xia, K., Xing, H., Ding, L., Gao, H., Liu, G., Deng, Z., 2019. Virtual decomposition based modeling for multi-DOF manipulator with flexible joint. IEEE Access 7, 91582–91592.

Xing, H., Ding, L., Gao, H., Li, W., Tavakoli, M., 2022. Dual-user haptic teleoperation of complementary motions of a redundant wheeled mobile manipulator considering task priority. IEEE Transactions on Systems, Man, and Cybernetics: Systems , 1–13.

Xing, H., Torabi, A., Ding, L., Gao, H., Deng, Z., Mushahwar, V.K., Tavakoli, M., 2021. An admittance-controlled wheeled mobile manipulator for mobility assistance: Human–robot interaction estimation and redundancy resolution for enhanced force exertion ability. Mechatronics 74, 102497.

Xing, H., Xia, K., Ding, L., Gao, H., Liu, G., Deng, Z., 2019. Unknown geometrical constraints estimation and trajectory planning for robotic door-opening task with visual teleoperation assists. Assembly Automation 39, 479–488.

Yuan, M., Manzie, C., Good, M., Shames, I., Gan, L., Keynejad, F., Robinette, T., 2020. A review of industrial tracking control algorithms. Control Engineering Practice 102, 104536.

Zhu, W.H., 2010. Virtual Decomposition Control - Toward Hyper Degrees of Freedom Robots. Springer Tracts in Advanced Robotics, Springer.

Zhu, W.H., Bien, Z., De Schutter, J., 1998. Adaptive motion/force control of multiple manipulators with joint flexibility based on virtual decomposition. IEEE Transactions on Automatic Control 43, 46–60.

Zhu, W.H., De Schutter, J., 2002. Experimental verifications of virtual-decomposition-based motion/force control. IEEE Transactions on Robotics and Automation 18, 379–386.

Zhu, W.H., Lamarche, T., 2007. Modular robot manipulators based on virtual decomposition control, in: IEEE International Conference on Robotics and Automation, pp. 2235–2240.

Zhu, W.H., Lamarche, T., Dupuis, E., Jameux, D., Barnard, P., Liu, G., 2013. Precision control of modular robot manipulators: The VDC approach with embedded FPGA. IEEE Transactions on Robotics 29, 1162–1179.

Zhuang, Y., Yao, S., Ma, C., Song, R., 2019. Admittance control based on emg-driven musculoskeletal model improves the human–robot synchronization. IEEE Transactions on Industrial Informatics 15, 1211–1218.